

FOUR-DIMENSIONAL MODELS OF FREE ELECTRON LASER AMPLIFIERS AND OSCILLATORS

J. Blau*, K. Cohn, W. B. Colson

Physics Department, Naval Postgraduate School, Monterey, CA 93943, USA

Abstract

New four-dimensional models of free electron lasers (FELs) are described, for both amplifier and oscillator configurations. Model validation and benchmarking results are shown, including comparisons to theoretical formulas and experiments.

INTRODUCTION

Over the past 25 years at the Naval Postgraduate School, we have developed a suite of computer programs to model free electron lasers [1, 2]. We have separate programs for different types of FELs (i.e., single-pass amplifiers or multi-pass oscillators) under various conditions (i.e., short or long pulses), with graphics optimized to understand the results for each type of FEL.

Our programs can be classified according to the number of dimensions in the model. The one-dimensional (1D) and two-dimensional (2D) programs run very rapidly on laptop and desktop computers. The 1D programs are helpful in visually understanding basic principles such as electron bunching, optical gain and saturation, and in many cases give good descriptions of FEL performance. The 2D programs are useful when longitudinal effects such as pulse slippage and desynchronism are dominant. The three-dimensional (3D) and four-dimensional (4D) programs typically run on multi-core or cluster computers, and are useful when transverse effects such as optical mode distortion are significant. Each of the programs produces extensive graphical output to enhance physical understanding and reveal trends.

This paper describes the new 4D models that we have developed over the past several years, taking advantage of advances in computer technology that enable these programs to run efficiently on readily available hardware such as Linux clusters. We also present results showing how we have validated and benchmarked the new models.

DESCRIPTION OF THE MODELS

Dimensionless Parameters

All of our models use dimensionless parameters that simplify the equations, provide intuitive insight, and generalize the results [3]. Longitudinal coordinates are normalized to the undulator length L , and transverse coordinates are normalized to a characteristic optical mode radius $\sqrt{L\lambda}/\pi$, where λ is the optical wavelength. The dimensionless time is defined by $\tau = ct/L$ where c is the speed of light.

Phase space coordinates follow the microscopic bunching of the electrons on the scale of an optical wavelength. The

electron phase is defined as $\zeta = (k + k_0)z - \omega t$ where $k = 2\pi/\lambda$ is the optical wavenumber, $k_0 = 2\pi/\lambda_0$ is the undulator wavenumber, λ_0 is the undulator period, $\omega = kc$ is the optical frequency, and z is the electron's position along the undulator axis at time t . The dimensionless phase velocity then becomes $v = d\zeta/d\tau = L[(k + k_0)\beta_z - k]$ where $\beta_z = v_z/c$.

The dimensionless undulator parameter is given by $K = eB\lambda_0/2\pi mc^2$, where B is the rms field strength, e is the electron charge and m is the electron mass (in cgs units). For most FELs, $K \sim 1$.

The dimensionless optical field amplitude is defined as $|a| = 4\pi NeKLE/\gamma^2 mc^2$, where N is the number of undulator periods, E is the electric field amplitude, and γ is the Lorentz factor. When $|a| \ll \pi$ the optical fields are weak and there is very little electron bunching. When $|a| \sim \pi$, there can be significant electron bunching, producing growth of the optical fields. When $|a| \gg \pi$, strong optical fields can cause many of the electrons to become trapped in closed phase space orbits, leading to the onset of saturation.

The optical fields are driven by the dimensionless current density, $j = 8N(e\pi KL)^2 \rho/\gamma^3 mc^2$, where ρ is the particle density. When $j \lesssim 1$, the weak-field gain is low, but when $j \gg 1$, the FEL can have high gain. A typical FEL oscillator has $j \sim 100$ and moderate weak-field gain. An FEL amplifier, with a much longer undulator, can have $j \sim 10^5$ and very high gain over a single pass.

Model Assumptions and Methods

The first 4D model that we developed in the early 1990s assumed the electron beam is well inside the optical mode [4]. In that case, all of the electrons in each longitudinal slice of the pulse interact with the same optical field, so the microscopic bunching is uniform across each slice. This assumption significantly reduces the computational and memory requirements for the simulation; for instance, instead of large 3D arrays for the electron phase ζ and phase velocity v , only 1D arrays are required.

Our new 4D models are more general, including the full evolution in (x, y, z, t) of the electrons and optical pulses. The programs are parallelized, with each process following an optical wavefront $a(x, y)$ and sample electrons for a single longitudinal slice of the optical pulse $a(z)$ along the undulator axis. In each slice, the optical wavefront is represented by the field amplitude and phase over a rectangular grid, and approximately 30,000 sample electrons are assigned transverse phase space coordinates $(x, \theta_x, y, \theta_y)$ in addition to their longitudinal phase space coordinates (ζ, v) . To reduce shot noise effects, a quiet start algorithm [5] is used to assign the initial phase space coordinates, taking

* blau@nps.edu

into account the emittance and energy spread of the electron beam. The effective charge corresponding to each sample electron is weighted by the current density profile of the electron pulse.

The number of transverse modes included in our models is limited only by the number of transverse grid points; typically a 300×300 grid is adequate, but in some cases a 1000×1000 grid is needed. The number of longitudinal slices determines the number of longitudinal modes; typically we use 100 slices, but in some cases several hundred slices are needed. The optical wavelength is allowed to evolve self-consistently.

On each time step, the electrons advance in phase space according to the relativistic Lorentz force equation, using a fourth-order Runge-Kutta method. Their transverse coordinates are updated according to the undulator betatron focusing. The undulator can have a step or linear taper starting at an arbitrary position; the Lorentz force equation is adjusted accordingly. The optical field evolves according to the parabolic wave equation, using a Fourier transform method. Electrons are continually passed from one optical slice to the next to account for pulse slippage. An important feature of our models is that they do not assume axial symmetry, so they can include arbitrary shifts and tilts of the electron beam and cavity mirrors with respect to the undulator axis to study the effects of misalignments on FEL performance [6].

A single-pass amplifier model was developed first. The initial optical field can be specified in terms of the seed laser parameters, or it can develop from spontaneous emission to simulate a SASE FEL. The initial electron beam can be described by statistical quantities such as the spread in positions and velocities along each dimension, or a particle tracking code such as PARMELA [7] or GPT [8] can be used to produce the initial electron distribution. Graphical output from the simulation includes the evolution of the optical power and gain along the undulator, the electron phase space, slices through the optical field in each dimension, the optical power spectrum, and a modal decomposition of the final optical field.

Next we developed multi-pass oscillator simulations. A transformation matrix is used to represent each mirror, with the radius of curvature determined by the cavity length and the dimensionless Rayleigh range. One of the mirrors can be partially transparent, or it can use hole out-coupling. Including mirrors within the program allows it run efficiently compared to other approaches that require exchanging the wavefronts with an external optics code on each pass. An expanding coordinate grid outside of the undulator [9] allows for the significant diffraction that occurs in a typical FEL oscillator, with a significant reduction in computation time and memory requirements.

The first oscillator model that we developed uses periodic boundary conditions, with the assumption that the pulse length is much greater than the slippage distance ($N\lambda$). The results of this model depend mainly on three key parameters: the dimensionless current density j , the cavity quality factor,

and the Rayleigh length. This model is useful for studying effects such as coherence evolution, the trapped-particle instability, the development of sidebands, and limit-cycle behavior.

We have recently developed another oscillator model that incorporates short pulses (comparable to the slippage distance). In this model, the longitudinal window is wide enough to contain the full extent of the electron and optical pulses as they evolve through the undulator, so it does not require periodic boundary conditions. Desynchronism is implemented by a steadily increasing shift of the optical pulse with respect to the electron pulse on each pass.

Graphical Output

To aid in analyzing the large amounts of data, our 4D simulations produce extensive graphical output. Figure 1 shows an example of simulation output for the Jefferson Laboratory infrared FEL oscillator [10]. The green shaded window at the top of the figure lists the dimensionless parameters used in the simulation. Near the middle on the left side of the figure is a plot labeled $a(x, 0, 0)$ which shows the amplitude of the optical field (blue) versus x at $y = z = 0$ at the beginning of the first pass; the narrower electron beam is superimposed in red. Directly above that is an intensity plot showing the evolution of this optical field profile over $n = 300$ passes through the undulator; here light blue corresponds to the largest optical field amplitude, and dark blue corresponds to zero field. The white lines indicate the $1/e$ value of the field amplitude, and the red dots indicate the $1/e$ value of the electron beam current at each pass. In the upper left is the final optical field profile; notice that the peak value, shown in the upper right corner of each plot, has increased from 6.7 to 26.6. Next to those plots is a similar series of plots, now showing the evolution of an optical field slice versus y at $x = z = 0$. These are virtually identical to the previous plots because the input parameters for this example had azimuthal symmetry (although our 4D model does not require that).

The next column of plots, labeled $a(0, 0, z)$, show the evolution of the electron and optical pulses versus z , at $x = y = 0$. The initial electron pulse (red) starts out slightly ahead of the optical pulse (blue), but ends up trailing the optical pulse by the slippage distance $N\lambda$ at the end of each pass. The z coordinate in these plots is normalized to the slippage distance. The evolution of the optical pulse over many passes depends on the interaction between the electron and optical pulses, and the desynchronism (or “detuning”) of the optical cavity [1].

In the upper right is a series of plots labeled $P(0, 0, \nu)$, showing the evolution of the optical power spectrum. This is obtained by taking the Fourier transform of the optical power $P(0, 0, z) = |a(0, 0, z)|^2$ at $x = y = 0$, as representative of the pulse spectrum. Notice that the power spectrum is initially peaked near resonance, $\nu = 0$, but shifts to a larger value $\nu \approx 8$ after $n \approx 200$ passes. This corresponds to a shift in the lasing wavelength of $\Delta\lambda/\lambda = \Delta\nu/2\pi N \approx 4\%$ as the FEL evolves from weak fields to saturation in strong

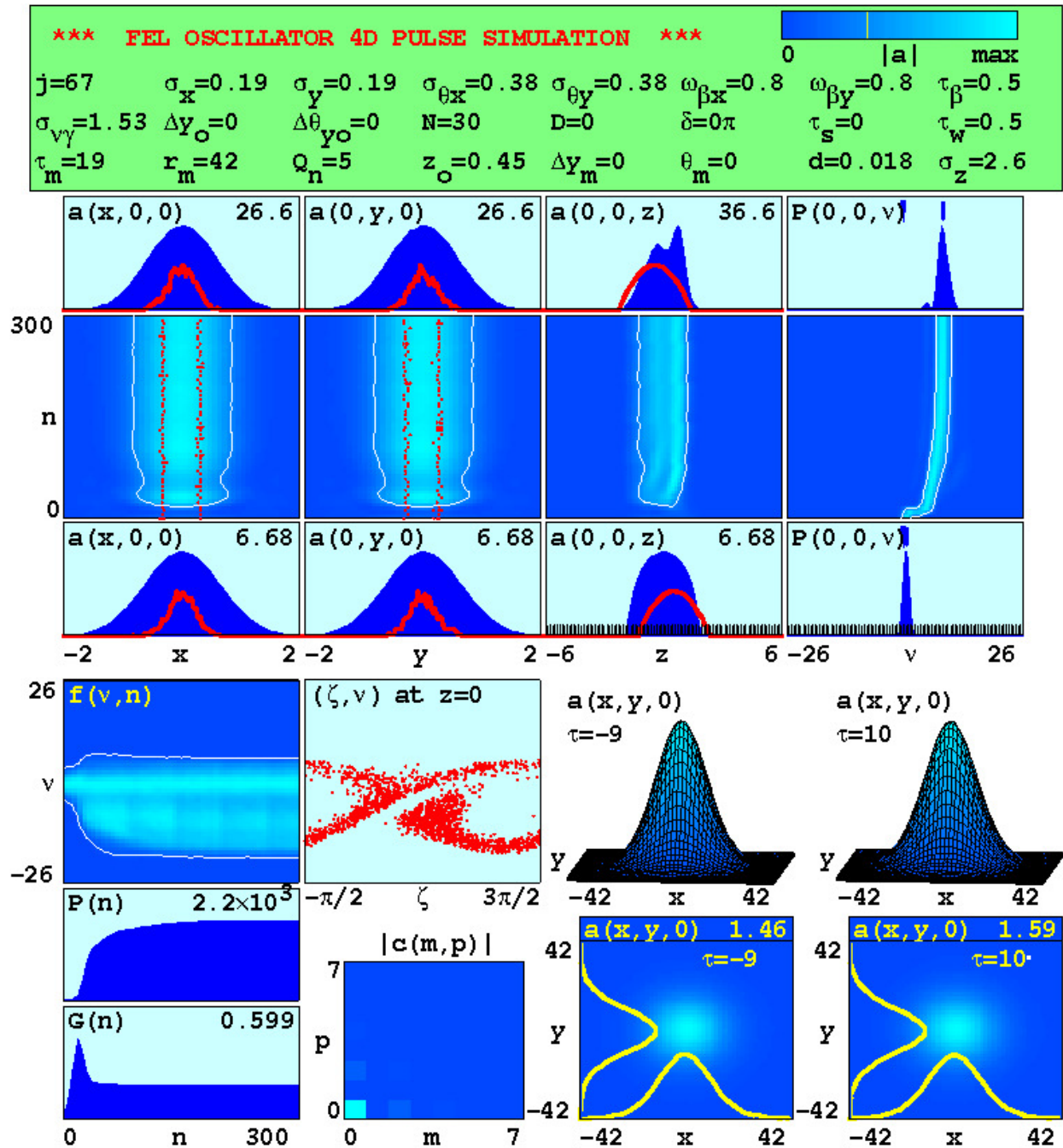


Figure 1: Output from a 4D simulation of the Jefferson Lab infrared FEL oscillator. The various plots are described in the text.

fields, a well-known effect predicted by FEL theory [1] and observed in many experiments.

In the lower half of the figure, the plot on the left labeled $f(v, n)$ shows the evolution of the electron phase velocity distribution. Notice that the electrons initially have a rather narrow phase velocity distribution due only to emittance and energy spread, but as they interact with the growing optical field in the undulator over many passes they develop a broader distribution in phase velocities. Next to that plot shows the final distribution of the electrons in phase space (ζ, v) at $z = 0$, indicating good bunching of the electron beam. In the bottom left of the figure are two plots showing the evolution of the optical power $P(n)$ and gain $G(n)$. Notice that the optical power saturates at a fixed value after $n \approx 200$ passes.

On the bottom of the figure near the center is a plot labeled $|c(m, p)|$, which depicts the modal composition of the optical wavefront, using a color scale to represent the values of the coefficients of the Hermite-Gaussian cavity modes. In this case, a light blue square at $p = m = 0$ indicates the wavefront is primarily in the fundamental (0,0) mode. This is confirmed by the four plots in the lower right of the figure, which show a nearly Gaussian optical wavefront $|a(x, y, 0)|$ at the left ($\tau = -9$) and right ($\tau = 10$) mirrors, in both 2D and 3D representations.

VALIDATION AND BENCHMARKING OF THE MODELS

First we will compare results from our simulations to well-known theoretical formulas. These formulas typically assume idealized cases, but they are useful to give rough approximations of FEL performance, and with careful choices of parameters they can be used to validate our models. We will also provide benchmarks by comparing simulation predictions to results from FEL experiments.

Weak-field Gain

In weak optical fields ($|a| \ll \pi$) and low current density ($j \lesssim 1$), the single-pass gain can be expressed as [1]

$$G = j \left(\frac{2 - 2 \cos \nu_0 - \nu_0 \sin \nu_0}{\nu_0^3} \right). \quad (1)$$

This formula assumes all of the electrons are injected with the same initial electron phase velocity ν_0 (i.e., no emittance or energy spread). It also assumes perfect overlap between the electron and optical beams, and it ignores effects such as diffraction, pulse slippage, and optical mode distortion. However, we can compare it to the results from our 4D amplifier model if we choose appropriate initial conditions. The electron and optical beams are given identical top-hat profiles with a large radius to minimize diffraction. Long, flat pulses are used to remove slippage effects. The resulting weak-field gain spectrum for $j = 1$ is shown in Fig. 2. The blue theory line corresponds to Eq. 1, and the red dots correspond to results from the 4D amplifier model. The results show excellent agreement between the theory

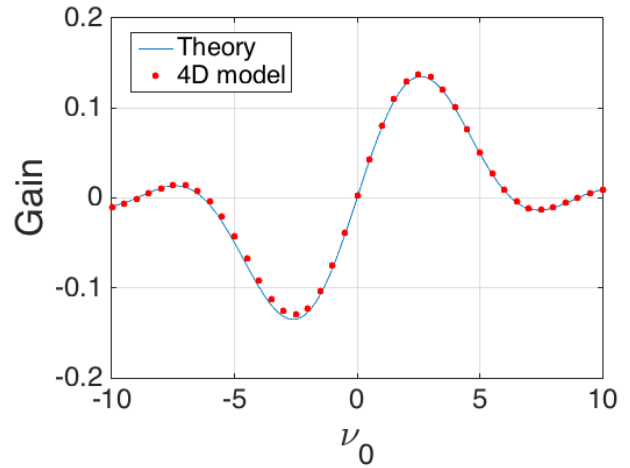


Figure 2: Weak field gain spectrum: single-pass gain vs. initial phase velocity ν_0 for a low-gain FEL ($j = 1$).

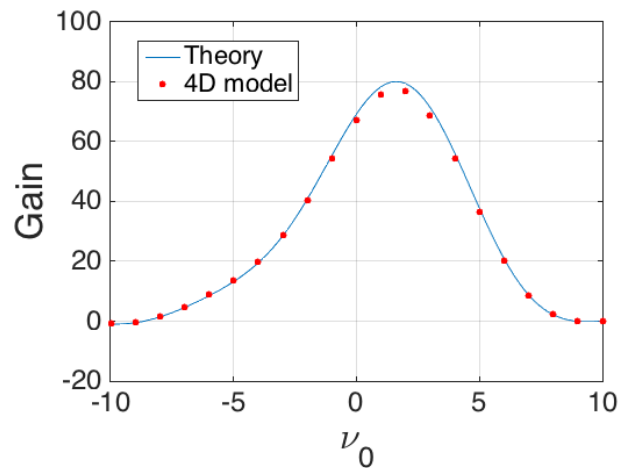


Figure 3: Weak field gain spectrum: single-pass gain vs. initial phase velocity ν_0 for a high-gain FEL ($j = 100$).

and the model for this idealized case. The slight differences are expected since Eq. 1 does not allow the optical fields to evolve self-consistently.

For a high-gain FEL ($j \gg 1$), Eq. 1 is no longer valid. Instead, the FEL integral equation described below can be used to estimate the gain. Now the gain spectrum is broader and more symmetric with a peak near resonance, $\nu_0 \approx 0$, as shown in Fig. 3. Here we have used $j = 100$; the blue theory line was obtained using the FEL integral equation, and the red dots are from our 4D amplifier model, with the same idealized conditions as before. Again, there is good agreement between the model and the theory.

For a high-gain FEL at resonance, $\nu_0 = 0$, the weak-field gain can be approximated as [1]

$$G \approx \frac{1}{9} e^{(j/2)^{1/3} \sqrt{3}} \quad (2)$$

Figure 4 shows results for gain versus current density j for our 4D model (red dots) compared to Eq. 2 (blue line).

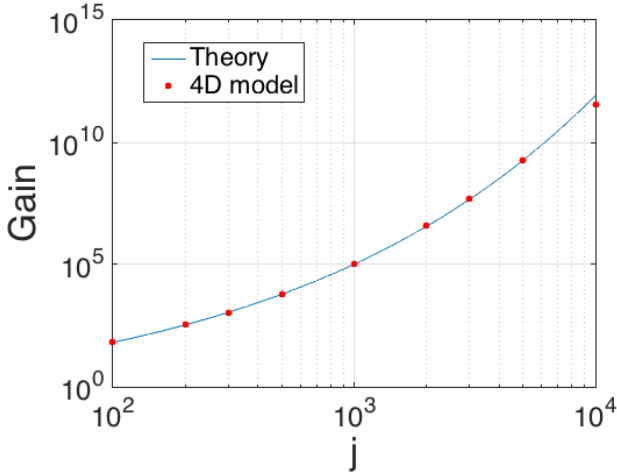


Figure 4: Weak-field gain vs. dimensionless current density j for high-gain FELs ($j \gg 1$) at resonance ($\nu = 0$).

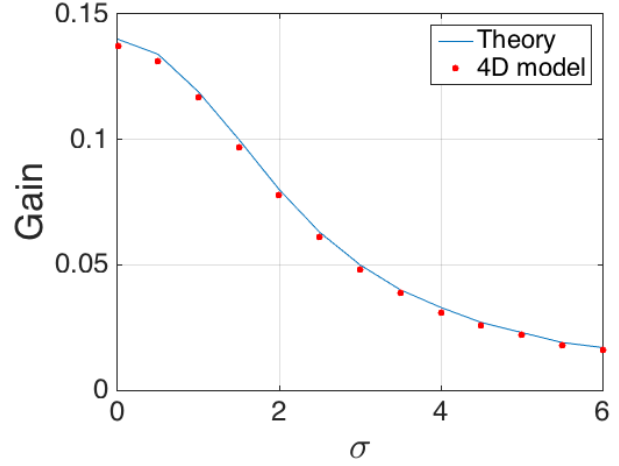


Figure 5: Weak-field gain vs. the rms spread σ in phase velocities due to an energy spread for a low-gain FEL ($j = 1$).

There is excellent agreement between the model and the theory over about 10 orders of magnitude change in gain (note the logarithmic scale on each axis).

The previous results all assume an idealized electron beam, with no energy spread or emittance. The effects of a realistic beam can be incorporated into the theory using the FEL integral equation [11, 12], which describes the evolution of the dimensionless, complex optical field,

$$\frac{da}{d\tau} = \frac{ij}{2} \int_0^\tau \tau' F(\tau') e^{-i\nu_0\tau'} a(\tau - \tau') d\tau' \quad (3)$$

where $F(\tau') = \int f(q) e^{-iq\tau'} dq$ is the characteristic function of the distribution $f(q)$ of electron phase velocities $v_i = v_0 + q$ about v_0 and $\int f(q) dq = 1$.

For example, if an electron beam has a Gaussian spread of energies, it will have a corresponding distribution in phase velocities $f(q) = \exp(-q^2/2\sigma^2)/\sqrt{2\pi}\sigma$ where $\sigma = 4\pi N\Delta\gamma/\gamma$ is the standard deviation. For a low-gain FEL, it is clear from Fig. 2 that when the spread in phase velocities is on the order of π , there will be significant gain degradation. Figure 5 shows the effect of increasing electron energy spread on FEL gain. The blue line corresponds to Eq. 3 and the red dots are results from our 4D model. Again, we see excellent agreement between the model and the theory.

Strong-field Gain

In strong optical fields, $|a| \gg \pi$, an analytic formula for gain is not available, but features of saturation can be explored and compared to a 1D model. Figure 6 shows results for 4D simulations of single-pass gain versus initial phase velocity v_0 and optical field amplitude a_0 . As the FEL evolves from weak fields $a_0 \approx 0$ up to moderately strong fields $a_0 = 20$, the peak gain decreases from $G \approx 13\%$ to $G \approx 3\%$, the gain spectrum $G(v_0)$ becomes broader and the peak shifts away from resonance, from $v_0 \approx 3$ to $v_0 \approx 5$. Simulations with our 1D model produce a nearly identical plot [1].

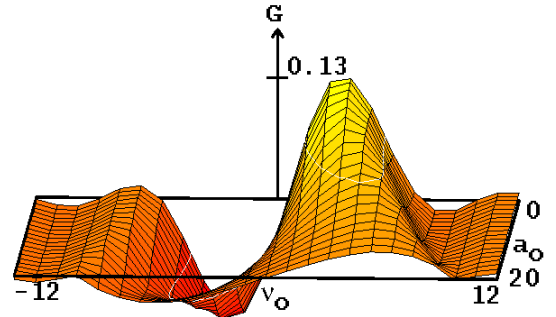


Figure 6: Results for 4D simulations of single-pass gain G vs. initial phase velocity v_0 and optical field amplitude a_0 for a low-gain FEL ($j = 1$).

Extraction

The FEL extraction η is defined as the ratio of the output optical power to the input electron beam power. Our simulations predict extraction by first determining the average change in phase velocity $\langle \Delta\nu \rangle$ of the sample electrons, then the corresponding extraction is calculated using $\eta = \langle \Delta\nu \rangle / 4\pi N$.

A low-gain FEL will saturate when the optical field amplitude reaches $|a| \approx 4\pi^2$. In that case, the trapped electrons will undergo an average phase velocity shift of $\langle \Delta\nu \rangle \approx 2\pi$, which gives an approximate theoretical extraction of $\eta_{th} \approx 1/2N$. Indeed, that is what our simulations invariably obtain for low-gain FELs, so long as the gain is above threshold. For example, the Jefferson Lab FEL oscillator has $N = 30$ periods, so the above formula predicts an extraction of $\eta_{th} \approx 1.67\%$. The actual experiment obtained extractions between 1.5% and 1.7% [10]. In our 4D simulation of this FEL shown in Fig. 1, the power evolution plot $P(n)$ near the lower left indicates saturation after $n = 200$ passes. The final phase velocity distribution $f(v, n)$

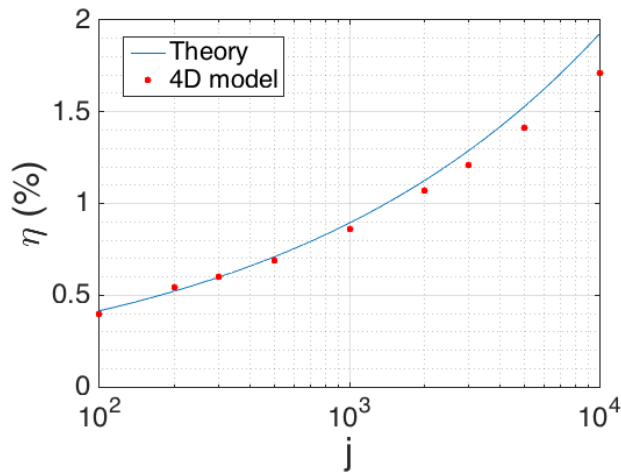


Figure 7: Extraction η vs. dimensionless current density j for high-gain FELs ($j \gg 1$) at resonance ($\nu = 0$).

shown above it yields an extraction of $\eta = 1.63\%$, in good agreement with the theory formula and the experimental results.

A high-gain FEL will saturate at a larger optical field amplitude $|a| \approx 2(j/2)^{2/3}$ [1], causing the trapped electrons to undergo an average phase velocity shift of $\langle \Delta\nu \rangle \approx 2\sqrt{2}(j/2)^{1/3}$. Assuming half of the electrons are trapped, the resulting theoretical extraction is

$$\eta_j \approx \frac{2\sqrt{2}(j/2)^{1/3}}{8\pi N}. \quad (4)$$

Figure 7 shows results for extraction versus current density for our 4D model (red dots) compared to Eq. 4 (blue line). There is good agreement between the model and the theory over a couple orders of magnitude change of the current density j . The slight differences at large j may be due to the assumption in Eq. 4 that half of the electrons are trapped.

Tapered Undulator

As an FEL approaches saturation, the electrons lose energy and are no longer in resonance with the optical field, thus reducing energy exchange. To further enhance extraction, the undulator can be tapered to restore resonance [13]. Typically this is done by a linear change in the undulator gap, resulting in a linear slope of the on-axis undulator field, $\Delta B/B$. This produces an effective acceleration of the electron phase velocity [1],

$$\delta = -4\pi N \left(\frac{K^2}{1+K^2} \right) \left(\frac{\Delta B}{B} \right) \left(\frac{1}{1-\tau_s} \right), \quad (5)$$

where τ_s is the dimensionless location of the taper start along the undulator axis (recall $\tau = 1$ corresponds to the end of the undulator). If half of the electrons remain trapped, the resulting extraction can be estimated as $\eta_\delta \approx \delta(1-\tau_s)/8\pi N$.

For example, the Brookhaven National Laboratory (BNL) seeded FEL amplifier had $N = 256$ periods and an undulator parameter of $K = 0.78$, with a 4% field taper along the

last 2.5m of the 10m long undulator [14]. The corresponding phase acceleration is thus $\delta \approx 63\pi$ starting at $\tau_s = 0.75$, and the estimated extraction is $\eta_\delta \approx 0.74\%$. The actual experiment obtained an extraction of $\eta \approx 0.8\%$.

Figure 8 shows the output of a 4D simulation of the BNL FEL amplifier. The various plots shown in this figure are similar to those in Fig. 1, except the evolution plots are now for a single pass through the undulator from $\tau = 0$ to $\tau = 1$. Since this is a high-gain FEL ($j = 7782$), the optical beam is “guided” along the axis near the electron beam, as seen in the evolution of the transverse profiles $a(x, 0, 0)$ and $a(0, y, 0)$ near the upper left of the figure. Beneath those plots, the evolution of the electron phase velocity, $f(\nu, \tau)$ shows the phase acceleration due to taper beginning at $\tau_s = 0.75$. The final phase space picture next to that indicates about half of the electrons remain trapped. The power and gain evolution plots in the lower left reveal a plateau at saturation $\tau \approx 0.75$, and then the power and gain continue to increase as the taper takes effect. Next to those plots, the modal composition plot $|c(m, n)|$ indicate the presence of numerous higher-order modes, as expected in a high-gain FEL. In this case, since there is no optical cavity, the basis set for the modal decomposition assumes the seed laser is in the fundamental (0,0) Hermite-Gaussian mode. Higher-order mode content is also observed in the strongly-peaked optical wavefront $a(x, y, 0)$ shown in the lower right at $\tau = 1$. The simulation obtained an extraction of $\eta = 0.84\%$, in good agreement with the theory formula and the experimental result.

CONCLUSION

Our new 4D models of FEL amplifiers and oscillators have been validated and benchmarked by comparison to theoretical formulas and experimental results. We have demonstrated excellent agreement between our simulations and the theory formulas for various regimes of FEL operation, and we have also shown good agreement with experimental results. We are now using the new 4D models to study the interaction between transverse and longitudinal effects, such as how diffraction affects desynchronization in short-pulse FELs.

ACKNOWLEDGMENT

The authors are grateful for support from the High Energy Laser Joint Technology Office.

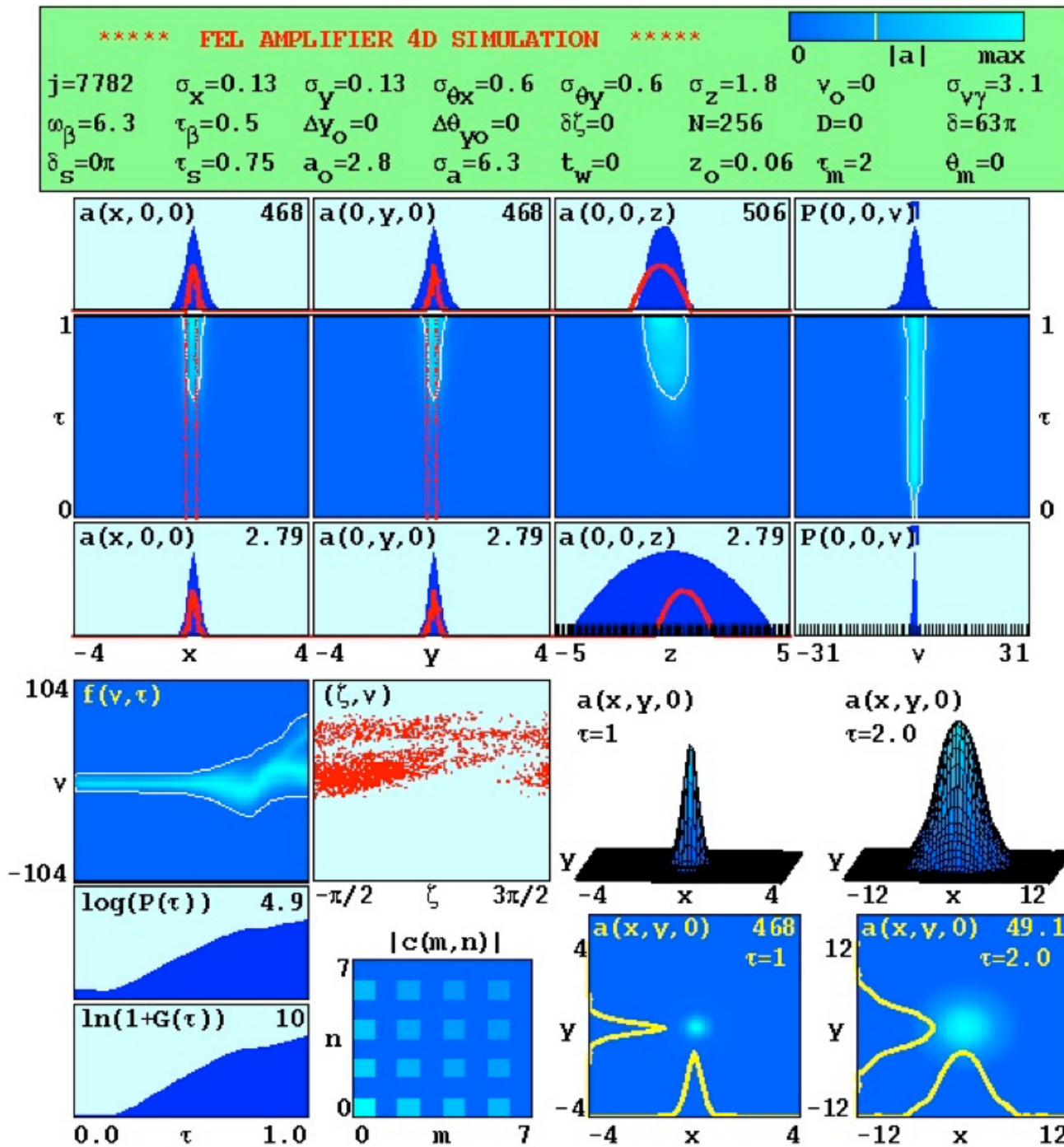


Figure 8: Output from a 4D simulation of the Brookhaven National Laboratory seeded FEL amplifier.

REFERENCES

- [1] W. B. Colson, in *Laser Handbook*, (Amsterdam: North-Holland, 1990), Chap. 5.
- [2] J. Blau, Ph.D. Thesis, Naval Postgraduate School, Monterey, CA (2002).
- [3] W. B. Colson and J. Blau, "Parameterizing Physics Effects in Free Electron Lasers", *Nucl. Instr. Meth. Phys. Res. A* 272, 386 (1988).
- [4] J. Blau and W. B. Colson, "Four Dimensional Simulations of the CEBAF Infrared Free Electron Laser", *Nucl. Instr. Meth. Phys. Res. A* 318, 717 (1992).
- [5] W. M. Fawley, "Algorithm for Loading Shot Noise Microbunching in Multidimensional, Free-Electron Laser Simulation Codes", *Phys. Rev. ST Accel. Beams* 5, 070701 (2002).
- [6] P. P. Crooker et. al., "Vibrations Effects in Short Rayleigh Length FELs", FEL'05, Stanford, CA, USA, August 2005.
- [7] L. M. Young and J. H. Billen, "The Particle Tracking Code PARMELA", PAC'03, Portland, OR, USA, May 2003.
- [8] M. J. de Loos and S. B. van der Greer, "General Particle Tracer: A New 3D Code for Accelerator and Beam Line Design", EPAC'96, Barcelona, Spain, June 1996.
- [9] R. L. Armstead, W. B. Colson and J. Blau, "Short Rayleigh Length Free Electron Laser Simulations in Expanding Coordinates", FEL'04, Trieste, Italy, August 2004.
- [10] S. Benson et. al., "High Power Operation of the JLAB IR FEL Driver Accelerator", PAC'07, Albuquerque, NM, USA, June 2007.
- [11] W. B. Colson, J. C. Gallardo and P. M. Bosco, "Free-Electron Laser Gain Degradation and Electron Beam Quality", *Phys. Rev. A* 34, 4837 (1986).
- [12] W. B. Colson and J. Blau, "Free Electron Laser Theory in Weak Optical Fields", *Nucl. Instr. Meth. Phys. Res. A* 272, 386 (1987).
- [13] N. M. Kroll, P. L. Morton and M. N. Rosenbluth, "Free-electron Lasers with Variable Parameter Wigglers", *IEEE J. Quant. Elect.* QE-17, 1436 (1981).
- [14] X. J. Wang et. al., "Efficiency and Spectrum Enhancement in a Tapered Free-electron Laser Amplifier", *Phys. Rev. Lett.* 103, 154801 (2009).